

Atomic-scale tandem regulation of anionic and cationic migration for long-life alkali metal batteries

Pan Xiong

Nanjing University of Science and Technology

Fan Zhang

University of Technology Sydney

Xiuyun Zhang

Yangzhou University

Yifan Liu

Nanjing University of Science and Technology

Yunyan Wu

Nanjing University of Science and Technology

Shijian Wang

University of Technology Sydney

Javad Safaei

University of Technology Sydney

Bing Sun

University of Technology Sydney <https://orcid.org/0000-0002-4365-486X>

Renzhi Ma

National Institute for Materials Science

Zongwen Liu

The University of Sydney <https://orcid.org/0000-0002-6434-1643>

Yoshio Bando

National Institute for Materials Science (NIMS) <https://orcid.org/0000-0002-6543-5529>

Takayoshi Sasaki

National Institute for Materials Science <https://orcid.org/0000-0002-2872-0427>

Xin Wang

Nanjing University of Science and Technology

Junwu Zhu

Nanjing University of Science and Technology <https://orcid.org/0000-0002-7518-9683>

Guoxiu Wang (✉ Guoxiu.Wang@uts.edu.au)

University of Technology Sydney <https://orcid.org/0000-0003-4295-8578>

Keywords: atomic-scale tandem regulation, anionic migration, cationic migration, batteries

Posted Date: February 2nd, 2021

DOI: <https://doi.org/10.21203/rs.3.rs-144424/v1>

License:  This work is licensed under a Creative Commons Attribution 4.0 International License.

[Read Full License](#)

Version of Record: A version of this preprint was published at Nature Communications on July 7th, 2021. See the published version at <https://doi.org/10.1038/s41467-021-24399-9>.

Abstract

Atomic-scale regulation of both cationic and anionic transport is of great significance in membrane-based separation technologies. Ionic transport regulation techniques could also play a crucial role in developing high-performance alkali metal batteries such as alkali metal-sulfur and alkali metal-selenium batteries, which suffer from the non-uniform transport of alkali metal ions and detrimental shuttling of polysulfide/polyselenide (PS) anions. These obstacles can cause severe growth of alkali metal dendrites and the irreversible consumption of active cathodes, leading to capacity decay and short cycling life. Herein, we report long-life alkali metal batteries enabled by atomic-scale tandem regulation of the migration of both alkali metal cations (Li^+/Na^+) and PS anions using negatively charged $\text{Ti}_{0.87}\text{O}_2$ nanosheets with Ti atomic vacancies. The shuttling of PS anions has been effectively eliminated via a robust electrostatic repulsion between the negatively charged nanosheets and PS anions. The negatively charged nanosheets can also regulate the migration of Li^+/Na^+ ions to ensure a homogeneous ion flux through efficient but light adhesion of Li^+/Na^+ ions within the nanosheets. The atomic Ti vacancies act as sub-nanometre pores to provide fast diffusion channels for Li^+/Na^+ ions. Therefore, eradication of PS shuttling and stable Li/Na-ion diffusion without compromising the fast transport of Li^+/Na^+ ions has been achieved for long-life alkali metal-sulfur and alkali metal-selenium batteries. This work provides a facile and effective strategy to regulate the transport of both cations and anions for developing advanced rechargeable batteries by using two-dimensional vacancy-enhanced materials.

Introduction

Rechargeable batteries beyond lithium-ion chemistry are considered as the most promising candidates for next-generation energy storage with low cost and high energy density¹⁻³. Among them, alkali metal batteries such as alkali metal-sulfur and alkali metal-selenium batteries have attracted much attention due to their high theoretical energy density⁴⁻⁷. However, multiple obstacles associated with both S and Se cathodes and alkali metal anodes have severely hindered their practical applications, especially, the unwanted shuttle effect of soluble polysulfide/polyselenide (PS) intermediates and the formation of alkali metal dendrites, which originate from the uneven migration of PS anions and alkali metal cations⁸⁻¹⁰. Considerable efforts have been devoted to mitigating these detrimental effects, including the use of composite S/Se cathodes^{7,11-13}, modified metal anodes^{14,15}, functionalized separators¹⁶⁻²³, and solid electrolytes²⁴⁻²⁶. Although these efforts have achieved some success by either impeding the shuttling effect or suppressing dendrite growth, the performance of batteries obtained so far is still far from satisfactory. Therefore, it is desirable to develop a multifunctional approach which can simultaneously regulate both cationic and anionic migrations for alkali metal batteries.

In a battery system, separator membranes provide channels for diffusion of both cations and anions. In alkali metal-S/Se batteries, nano- and micro-porous polyolefin-based membranes such as polypropylene (PP), are commonly used as separators. However, these porous membranes with a large pore size have a limited selective effect on the transportation of ions²⁷. The flow of both alkali metal ions (such as Li^+ and

Na⁺) and PS anions can be considerably throttled when using such separator membranes. On the one hand, small but cumulative diffusion of PSs usually causes irreversible loss of sulfur, resulting in poor cycle life of batteries. Furthermore, unregulated diffusion of alkali metal ions induces inhomogeneous alkali metal deposition, leading to possible formation of metal dendrites and short-circuiting. Hence modification of separators could be a straightforward way to control the migration of both alkali metal cations and PS anions to simultaneously eliminate the formation of metal dendrites and the shuttle effect of PSs. So far, various functional materials have been employed to modify separators, including carbon materials^{17,20,28-33}, metal-based oxides^{21,23,34,35}, sulfides³⁶⁻³⁸, carbides³⁹ and hydroxides^{40,41}, and metal-organic frameworks (MOFs)^{16,19,42-46}. However, to effectively suppress PS shuttling, most of the functional layers used to date have a high weight density and a large thickness. These inevitably place a severe burden on the weight and useable volume of the whole cell, which subtracts from the targeted high energy densities of alkali metal-S/Se batteries. More importantly, the retarding layer is an extra barrier to ion transfer, which causes large interfacial resistance and suppresses the transport of alkali metal cations. Therefore, an ideal functional layer should be as thin as possible to maximize alkali metal cation transport without compromising the ability to prevent PS shuttling, thus forming a selective ionic sieve with high permeability for alkali metal ions.

Permselective ionic sieves have been widely applied in membrane-based separation technologies mainly based on the basic size-sieving effect and electrical interaction between ions and the membrane⁴⁷⁻⁴⁹ (Fig. 1a). Ions/molecules with sizes smaller than the pore size of the membrane can pass, while the ions with larger volumes are selectively excluded. When significant electrical interactions are present, charged membrane surfaces repel identically charged ions while attracting oppositely charged ions which may then permeate through the membrane. Because the flux of ions is inversely proportional to the membrane thickness, an 'ultimate' membrane would be a one-atom-thick layer with well-defined nanopores⁵⁰. Therefore, two-dimensional (2D) porous materials with an atomic-scale thickness have attracted extensive interest⁵¹⁻⁵³. Since 2D atomically-thin nanosheets with sub-nanometer pores could act as a highly selective and permeable separator, they are highly desirable for long-life alkali metal-S/Se batteries. Several 2D nanosheet materials had been investigated, including graphene oxide (GO)/reduced graphene oxide (rGO), MoS₂ and MXenes. The membranes/separators of this type that have been studied were generally thick layers ranging from several micrometers to hundreds of micrometers^{29,36,39}. The PS shuttling effects were mitigated owing to the steric hindrance effect, but the diffusion of Li or Na-ions was also hindered. Furthermore, without nanopores, the Li⁺/Na⁺ ions could only migrate through gaps between layers of the materials. Therefore, fabrication of 2D atomically thin membranes with sub-nanometer pores is a niche strategy for attaining higher performance alkali metal batteries (Fig. 1b). To the best of our knowledge, this has not yet been reported. Sub-nanopores could efficiently exclude large PS anions while allowing small Li⁺/Na⁺ ions to rapidly pass through. The atomic-thin membrane would minimize main transit lengths. Moreover, using negatively charged nanosheets can repel anionic PS ions and thus enhance the suppression of the shuttle effect while simultaneously facilitating the diffusion of Li⁺/Na⁺ cations via the membrane-ion electrical interactions.

Here, we report 2D negatively charged titania ($\text{Ti}_{0.87}\text{O}_2$) nanosheets with Ti atomic vacancies as a selective ionic sieve in alkali metal batteries. The $\text{Ti}_{0.87}\text{O}_2$ nanosheets, delaminated from their parent layered oxides, are single-crystal unilamellar nanosheets with a thickness of 0.75 nm. By a facile filtration method, these unilamellar layers were layer-by-layer self-assembled onto commercial PP separators with a controlled ultralow weight density of 0.016 mg cm^{-2} and an average thickness of $\sim 80 \text{ nm}$. The intrinsic Ti atomic vacancies can act as sub-nanometer pores, making the $\text{Ti}_{0.87}\text{O}_2$ layer a promising atomically-thin membrane for simultaneously regulating the migration of Li^+/Na^+ cations and PS anions at an atomic scale. At the anode side of alkali metal batteries (Fig. 1c), the negatively charged nanosheets offer strong electrostatic interaction for the efficient adhesion and homogeneous distribution of Li^+/Na^+ ion flux, resulting in effective elimination of Li/Na dendrite growth. Moreover, the rich Ti vacancies and atomic-scale thickness provide fast pathways for the diffusion of Li^+/Na^+ cations. At the S/Se cathode side of alkali metal batteries (Fig. 1d), the negatively charged $\text{Ti}_{0.87}\text{O}_2$ nanosheets with a high negative charge density effectively exclude PS anions via a strong electrostatic repulsion effect. As a result, when applied in Li-S, Li-Se and Na-Se batteries, the $\text{Ti}_{0.87}\text{O}_2$ modified separators enable long-term cycling stability. Flexible Li-S pouch cells were fabricated and exhibited stable cycling performance under different bending conditions, demonstrating the potential of the $\text{Ti}_{0.87}\text{O}_2$ nanosheets for practical applications.

Results

Fabrication and characterizations of the functional $\text{Ti}_{0.87}\text{O}_2$ /PP separator

Negatively charged $\text{Ti}_{0.87}\text{O}_2$ nanosheets in the form of $\text{Ti}_{0.87}\square_{0.13}\text{O}_2$, where \square represents the Ti vacancies, were prepared by soft chemical exfoliation of layered lepidocrocite-type titanate crystals^{54,55}. As illustrated in Fig. 2a, the nanosheet is a single-crystal-like 2D ultrathin monolayer (0.75 nm thickness) with a high density of Ti vacancies⁵⁶. The size of the single-Ti atomic vacancy is $\sim 0.2 \text{ nm} \times 0.2 \text{ nm}$ ^{56,57}, which is larger than a Li^+ ion (0.9 Å diameter) or Na^+ ion (1.2 Å diameter) but smaller than a PS anion. Therefore, the Ti vacancies may work as migration-aids for Li^+/Na^+ ions and obstacle channels for PS anions, respectively. Atomic force microscopy (AFM) analysis (Fig. 2b) confirmed that the exfoliated $\text{Ti}_{0.87}\text{O}_2$ nanosheets are unilamellar sheets with a uniform thickness of approximately 1.1 nm. Transmission electron microscopy (TEM) images as shown in Fig. 2c display a flat and transparent sheet-like morphology, which is consistent with the AFM observation. Selected area electron diffraction (SAED) (inset in Fig. 2c) indicates the mono-crystalline nature of the $\text{Ti}_{0.87}\text{O}_2$ nanosheets. Figure 2d shows an atomic-resolution high-angle annular dark-field scanning transmission electron microscopy (HAADF-STEM) image of a $\text{Ti}_{0.87}\text{O}_2$ nanosheet, where the Ti vacancies can be clearly visualized^{58,59}. The Ti vacancies endow the obtained nanosheets negative charges, which has been confirmed by zeta-potential measurements (Figure S1). X-ray absorption fine spectroscopy (XAFS) was conducted to further investigate the structural characteristics of the defect-containing nanosheets. Figure 2e shows the Ti K-edge X-ray absorption near-edge structure (XANES) spectra of commercial rutile TiO_2 and $\text{Ti}_{0.87}\text{O}_2$

nanosheets. The pre-edge peak at ~ 4981 eV represents transitions of core electrons into O 2p states that are hybridized with the empty Ti 4p state^{60,61}. The intensity of this peak for the $\text{Ti}_{0.87}\text{O}_2$ nanosheets was obviously increased compared to that of rutile TiO_2 , elucidating a decreased electron number of the O 2p–Ti 4p hybrid orbitals. This result indicates the presence of lattice O atoms with unsaturated coordination, which should be attributed to the presence of nearby Ti vacancies⁶². Moreover, the Ti K-edge extended XAFS (EXAFS) $k^3\chi(k)$ oscillation curve of the $\text{Ti}_{0.87}\text{O}_2$ nanosheets exhibited a slight intensity decrease compared to rutile TiO_2 (Fig. 2f), which also confirms the presence of Ti vacancies^{61,62}. The interatomic distances of rutile TiO_2 and $\text{Ti}_{0.87}\text{O}_2$ nanosheets were determined through Fourier transformed Ti K-edge EXAFS data (Fig. 2g). The first major coordination peak corresponds to the nearest Ti–O bond in the first coordination shell. The peak intensity for the $\text{Ti}_{0.87}\text{O}_2$ nanosheets obviously decreased relative to the TiO_2 samples, which further verifies the presence of Ti vacancies^{61,62}.

Functional $\text{Ti}_{0.87}\text{O}_2/\text{PP}$ separators were fabricated by a facile vacuum filtration method (Figure S2). Compared to the porous surface of PP separators (Figure S3), $\text{Ti}_{0.87}\text{O}_2/\text{PP}$ separators showed a homogeneous morphology with uniform surface coverage by $\text{Ti}_{0.87}\text{O}_2$ nanosheets (Fig. 2h). As shown in Figure S4, a broad (010) diffraction peak of lamellar $\text{Ti}_{0.87}\text{O}_2$ was observed, which is the same as the nanosheets being self-assembled onto commercial PP separators. The weight density and thickness of the $\text{Ti}_{0.87}\text{O}_2$ functional layers in the resultant $\text{Ti}_{0.87}\text{O}_2/\text{PP}$ separator can be conveniently controlled by directly adjusting the volume of the nanosheet suspensions used in the vacuum filtration process. Figure S5 shows X-ray diffraction (XRD) data of $\text{Ti}_{0.87}\text{O}_2/\text{PP}$ separators with different weight densities. As the weight density increased, the XRD peaks became more intense, with increasing thickness of the $\text{Ti}_{0.87}\text{O}_2$ layer. A cross-sectional scanning electron microscopy (SEM) image (Fig. 2i) shows a thickness of approximately 80 nm. Cross-sectional TEM images displayed parallel lamellar fringes (Fig. 2j), further revealing the layer-by-layer assembly of the $\text{Ti}_{0.87}\text{O}_2$ nanosheets. The fringe spacing was measured to be ~ 1.1 nm, which is consistent with the basal spacing in the XRD pattern (Figure S4). It should be noted that the weight and thickness of the $\text{Ti}_{0.87}\text{O}_2$ layer was only approximately 0.32% and 1.5% of those of the commercial PP separator (thickness, 25 μm ; weight, 2.16 mg; diameter, 16 mm), respectively. Such a low weight density and ultrathin thickness have not been reported previously, to the best of our knowledge (Table S1). The as-prepared atomically-thin $\text{Ti}_{0.87}\text{O}_2$ layers can permit significantly high cation fluxes, which results in fast Li/Na-ion diffusion. The morphology and cross-sectional characteristics of $\text{Ti}_{0.87}\text{O}_2/\text{PP}$ separators with relatively high weight densities of 0.032 and 0.096 mg cm^{-2} were also investigated (Figures S6–S9). Homogeneously stacked layers with thicknesses of approximately 150 and 460 nm were obtained, respectively.

For comparison, anatase TiO_2/PP and GO/PP separators with the same weight density of 0.016 mg cm^{-2} were fabricated (Figures S2 and S4). As shown in Figure S10, the anatase TiO_2 nanoparticles did not disperse uniformly when coated onto PP surfaces. Only a limited part of the PP surfaces was covered by the aggregates of anatase TiO_2 nanoparticles. This is clearly different from the charged nanosheets in

suspensions where aggregation has been prevented due to Coulombic repulsion (neutral nanoparticles with high surface energy are prone to aggregate). As another negatively charged nanosheet material, GO was able to uniformly coat on the surface of PP separators (Figure S11). A slightly larger thickness of approximately 120 nm was observed for the GO/PP separator (Figure S12), compared with the $\text{Ti}_{0.87}\text{O}_2$ /PP separators. This matches the calculated result based on an ideal 2D weight density in the lateral dimensions of GO and $\text{Ti}_{0.87}\text{O}_2$ monolayers (Figure S13).

The coating of atomically-thin $\text{Ti}_{0.87}\text{O}_2$ layer brings several advantages to improve the electrochemical performance of a separator membrane. As shown in Figure S14, after being placed on a hot plate and heated at 120°C for 10 min, the $\text{Ti}_{0.87}\text{O}_2$ /PP film retained its original geometrical shape, while the pristine PP film tended to shrink. The improved thermal stability of the $\text{Ti}_{0.87}\text{O}_2$ /PP would enhance the safety of batteries in practical applications. Figure S15 shows the contact angles of electrolyte on the PP and $\text{Ti}_{0.87}\text{O}_2$ /PP separators. A smaller contact angle was observed on the $\text{Ti}_{0.87}\text{O}_2$ /PP separators than that on PP separators, suggesting a better wettability of the $\text{Ti}_{0.87}\text{O}_2$ /PP separators by electrolyte. Besides this effect, the as-prepared $\text{Ti}_{0.87}\text{O}_2$ /PP separators showed high stability under various degrees of mechanical bending (Figure S16). As shown in Figures S17-S19 and Fig. 2k, the Li^+ ion conductivity (see the Experimental details in the Supplementary Information) of the $\text{Ti}_{0.87}\text{O}_2$ /PP separators ($3.81 \times 10^{-1} \text{ mS cm}^{-1}$) was higher than that of the bare PP ($3.05 \times 10^{-1} \text{ mS cm}^{-1}$) and anatase TiO_2 /PP separators ($2.46 \times 10^{-1} \text{ mS cm}^{-1}$), and over three times higher than GO/PP separators ($1.17 \times 10^{-1} \text{ mS cm}^{-1}$). The Li-ion transference numbers were also determined, as shown in Figure S20 (see the Experimental details in the Supplementary Information). Compared to other functional layers, the Li^+ ion transference number increased significantly from 0.36 for bare PP to 0.55 for $\text{Ti}_{0.87}\text{O}_2$ /PP with a weight density of 0.016 mg cm^{-2} (Fig. 2k and Figure S21). Generally, covering open pores of pristine separators will increase the tortuosity of ion movement, leading to reduced Li-ion diffusion. However, the above testing results demonstrated that $\text{Ti}_{0.87}\text{O}_2$ nanosheets can facilitate Li-ion migration. Because the $\text{Ti}_{0.87}\text{O}_2$ layers are negatively charged with cation vacancies, the electrostatic attraction force between $\text{Ti}_{0.87}\text{O}_2$ nanosheets and Li^+ -cations facilitates the migration of Li ions towards the membrane with subsequent diffusion through the membrane. Similar phenomenon was also observed in other recent papers^{63,64}, in which Li^+ ions were observed to pass through the open channels of TaO_3 nanosheets with a mesh structure. The Ti vacancies further provide an expressway for rapid transportation of Li^+ ions in addition to the conventional interlayer galleries between the $\text{Ti}_{0.87}\text{O}_2$ sheets⁶⁴. Besides these effects, the atomically-thin size scale of the $\text{Ti}_{0.87}\text{O}_2$ layers is also favorable for fast Li-ion diffusion.

Dendrite-free alkali metal anodes

Benefiting from the merits mentioned above, $\text{Ti}_{0.87}\text{O}_2$ /PP separators are promising for regulating alkali metal ion flux in electrolyte and facilitating homogenous alkali metal deposition. Asymmetric Li||Cu half cells with various separators were fabricated to evaluate the cycling performance of Li metal anodes during repeated deposition and stripping. As shown in Fig. 3a, the cell with the $\text{Ti}_{0.87}\text{O}_2$ /PP separator

exhibited a steady Coulombic efficiency above 96.5% with stable plating/stripping voltage profiles for more than 100 cycles (Fig. 3b). In contrast, the cells with the bare PP (Fig. 3c), anatase TiO_2 /PP (Figure S22) and GO/PP separators (Figure S23) displayed a gradually increased voltage hysteresis and severely fluctuating Coulombic efficiency, which can be ascribed to the non-uniform Li deposition, and the formation of mossy or dendritic Li on the surface of Li metal anodes. Symmetric Li||Li cells were assembled to further investigate the superiority of $\text{Ti}_{0.87}\text{O}_2$ /PP separators for stabilizing Li metal anodes. As shown in Fig. 3d, the cell with the $\text{Ti}_{0.87}\text{O}_2$ /PP separator delivered an extended cyclability with stable voltage plateaus (Figs. 3e-3g) for over 300 h at a current density of 2 mA cm^{-2} with an area capacity of 1 mAh cm^{-2} . In sharp contrast, the cell with the PP separator exhibited a gradual increase in voltage hysteresis (Figs. 3d-3f). A similar phenomenon was found for regulating Na deposition and suppressing Na dendrite growth using $\text{Ti}_{0.87}\text{O}_2$ /PP separators. Figure S24 shows the Coulombic efficiencies of asymmetric Na||Cu cells with PP and $\text{Ti}_{0.87}\text{O}_2$ /PP separators. The corresponding voltage profiles of Na plating/stripping in Na||Cu half cells with PP and $\text{Ti}_{0.87}\text{O}_2$ /PP separators are shown in Figures S25 and S26, respectively. The average Coulombic efficiency of the cell with the $\text{Ti}_{0.87}\text{O}_2$ /PP separator is about 98.8% for 200 cycles. In contrast, the Coulombic efficiency of the cells with the bare PP decreased below 91% in 150 cycles.

The morphology of the cycled Li anodes in symmetric cells was investigated to clarify the effect of the $\text{Ti}_{0.87}\text{O}_2$ nanosheets on the suppression of Li dendrite formation. As shown in Figures S27 and S28, the loosely-stacked mossy Li with a highly porous structure has been observed on the Li anodes from cells with bare PP separators. In contrast, when a $\text{Ti}_{0.87}\text{O}_2$ /PP separator was used, the surfaces of the Li metal anodes were still compact without obvious mossy Li (Figures S29 and S30). This result demonstrates that the $\text{Ti}_{0.87}\text{O}_2$ nanosheets can facilitate homogeneous Li^+ ion flux, giving rise to uniform Li deposition. Additionally, AFM Young's modulus mappings revealed that $\text{Ti}_{0.87}\text{O}_2$ /PP separators exhibited a modest modulus of around 60 MPa, (Figure S31, see the Experimental details in the Supplementary Information), meeting the requirement for suppressing the growth of Li dendrites⁶⁵.

Theoretical calculations were conducted to investigate the diffusion properties of Li^+ ions through anatase TiO_2 (Fig. 4a), lepidocrocite-type TiO_2 without Ti vacancies (Fig. 4b) and Ti-defect-containing $\text{Ti}_{0.87}\text{O}_2$ (Fig. 4c). Figure 4d shows the transfer profiles of single Li^+ ions passing through these layers. For anatase TiO_2 and lepidocrocite TiO_2 , potential energy barriers are as high as 4.83 and 7.06 eV, respectively. This indicates that it would be challenging for a Li^+ ion to diffuse through them. After introducing a Ti vacancy, the energy barrier of the $\text{Ti}_{0.87}\text{O}_2$ monolayer radically decreased to 0.75 eV, which is comparable to, or even lower than, that of defective graphene⁶⁶. Besides these lattice averages, the electronic structure of $\text{Ti}_{0.87}\text{O}_2$ might also induce lowered energy barriers. The charge density distribution on a $\text{Ti}_{0.87}\text{O}_2$ lattice with a single Ti cationic defect is shown in Fig. 4e. It can be seen that the charge density around the Ti vacancy can significantly increase the charge attraction for a Li^+ ion, reducing the electrostatic charge overlapping, and weakening any Coulombic repulsion between a Li^+ ion

and the $\text{Ti}_{0.87}\text{O}_2$ lattice, thus resulting in a lower diffusion barrier for Li^+ ions. To further visualize the effects of defective nanosheets on the Li-ion transportation process, two kinds of thin-layer models were constructed by restacking the conventional nanosheets and defective nanosheets, respectively (Figure S32). In the case of the restacked thin layer of conventional nanosheets, the gaps between the adjacent nanosheets were the only pathways for Li^+ ion transport. Thus, a non-uniform distribution of Li^+ ions was formed (Fig. 4f). In contrast, in the restacked thin layer of cation-defect nanosheets, the Li^+ ions could be uniformly redistributed. This can be explained by the fact that Li^+ ions migrate through not only the gaps between layers but also the defects within individual layers, resulting in a uniform distribution of Li-ion flux (Fig. 4g). Although the above idealized models cannot fully reflect all the aspects of real circumstances (especially once electrolyte interactions are introduced into the scenarios), the theoretical calculation and simulation results demonstrate the superiority of the cation-defect nanosheets for facilitating Li^+ ion transport.

We propose a possible mechanism on the formation of dendrite-free alkali metal (Li/Na) anodes by using the negatively charged $\text{Ti}_{0.87}\text{O}_2$ nanosheets with atomic Ti vacancies (Figure S33). Upon discharging, solvated Li^+ ions in liquid electrolyte diffuse to the anode side. The negatively charged $\text{Ti}_{0.87}\text{O}_2$ nanosheets could attract numbers of Li^+ ions and facilitate the de-solvation process of the solvated Li^+ ions before deposition, leading to a small energy barrier for deposition^{67,68}. Then, the desolvated Li^+ ions diffuse through the Ti atomic vacancies. Given the homogenized Ti atomic vacancies of the as-prepared $\text{Ti}_{0.87}\text{O}_2$ nanosheets, a uniform Li^+ flux has been achieved. Consequently, a dendrite-free Li anode with a smooth deposition is formed. However, in the absence of $\text{Ti}_{0.87}\text{O}_2$ layers, a large energy barrier is needed during the de-solvation process^{67,68}. The distribution and transport of Li^+ ions are inhomogeneous and then form Li tips. Subsequently, Li^+ ions tend to accumulate at preferentially formed Li tips, resulting in severe dendrite growth (Figure S34).

Elimination of polysulfide/polyselenide (PS) shuttling

In addition to ion re-distribution for a uniform alkali metal deposition, negatively charged $\text{Ti}_{0.87}\text{O}_2$ can also act as a protective barrier to inhibit the shuttle effect of PS anions. Taking polysulfides as an example, permeation measurements were conducted to evaluate the permeation resistance of $\text{Ti}_{0.87}\text{O}_2/\text{PP}$ separators for minimizing the diffusion of PS anions (see the Experimental details in the Supplementary Information). The diffusion of Li_2S_6 was observed when use PP (Fig. 5b) and anatase TiO_2/PP separators (Figure S35a) within 1 h. In contrast, the GO/PP and $\text{Ti}_{0.87}\text{O}_2/\text{PP}$ separators were able to suppress the diffusion of PSs. However, as time elapsed, PSs were still able to pass through the GO/PP separators (Figure S35b). Only the $\text{Ti}_{0.87}\text{O}_2/\text{PP}$ separator demonstrated a stable blocking effect towards PSs, lasting up to 10 h (Fig. 5a). Both GO and the $\text{Ti}_{0.87}\text{O}_2$ nanosheets are negatively charged and thus could suppress the shuttling of the negatively charged PS anions via electrostatic repulsion. The different capabilities of GO and $\text{Ti}_{0.87}\text{O}_2$ for preventing the shuttling of PS anions should ascribed to their negative charge densities. Based on theoretical calculations (Figure S36), $\text{Ti}_{0.87}\text{O}_2$ nanosheets have a

negative charge density of 1.46 C m^{-2} , which is over 20 times higher than that of GO (0.064 C m^{-2})⁶⁹. Therefore, the $\text{Ti}_{0.87}\text{O}_2$ nanosheets with a much higher negative charge density can more effectively inhibit PS shuttling than GO layers. DFT calculations were performed to further elucidate the electrostatic repulsion between PS anions and $\text{Ti}_{0.87}\text{O}_2$ nanosheets (Figs. 5c-5f). Similar calculation methods were also conducted on anatase TiO_2 and GO sheets (Figures S37 and S38). As shown in Fig. 5g, the $\text{Ti}_{0.87}\text{O}_2$ displayed much higher repulsion energies than anatase TiO_2 or GO for all PS species.

Ex situ Raman spectroscopy was measured to gain further insights into the suppression of PS shuttling by the $\text{Ti}_{0.87}\text{O}_2$ nanosheets. Li-S coin cells were disassembled at a given voltage during the charge/discharge processes. We characterized the surfaces of the separators which had been in contact with lithium anodes. Figures 5h and 5i show the Raman spectra of the PP and $\text{Ti}_{0.87}\text{O}_2/\text{PP}$ separators, respectively, retrieved from Li-S batteries. For the PP separator (Fig. 5h), three characteristic Raman peaks of S_8^{2-} (at $\sim 150, 220, \text{ and } 470 \text{ cm}^{-1}$) were observed in the initial stage of the discharge process, associated with the formation of long-chain PSs. The Raman peaks of S_8^{2-} gradually decreased as the discharge reaction proceeded. Meanwhile, Raman peaks at ~ 260 and 415 cm^{-1} emerged, which correspond to the short-chain PSs of S_4^{2-} and S_5^{2-} . At the end of the discharge process, strong characteristic peaks of S_4^{2-} and S_5^{2-} were observed. This clearly indicates that the PSs shuttled through the PP separator from the cathode side and then deposited on the PP separator facing the anode side. Similarly, during the charging process, strong Raman signals of various PSs were observed. In contrast, for the $\text{Ti}_{0.87}\text{O}_2/\text{PP}$ separator (Fig. 5i), almost no Raman signals of PS species were detected throughout the entire discharge and charge processes, indicating effective inhibition of PS shuttling. To observe the inhibition of PS shuttling and stabilization of Li metal anodes, the cycled cells were disassembled and the sides of Li metal anodes facing the separators were checked. As shown in Figure S39a, yellow polysulfides were observed on the Li anodes in the cells with PP separators. For the cell with $\text{Ti}_{0.87}\text{O}_2/\text{PP}$ separators, almost no yellow species were observed and the cycled Li metal still exhibited a bright metallic lustre (Figure S39b). All these results confirmed that the PS shuttling and the growth of Li dendrites has been successfully eliminated when using $\text{Ti}_{0.87}\text{O}_2/\text{PP}$ separators. A molecular dynamic simulation further confirmed the inhibition of the PS shuttling and regulation of Li ion transport through the Ti vacancies (Movie S1).

Electrochemical performances

The electrochemical performances of $\text{Ti}_{0.87}\text{O}_2/\text{PP}$ separators in Li-S batteries were tested using a carbon black/S composite cathode. Typical cyclic voltammogram (CV) curves of a Li-S cell with a $\text{Ti}_{0.87}\text{O}_2/\text{PP}$ separator showed distinct reduction/oxidation peaks, which correspond to the conversion reactions of sulfur cathodes (Figure S40). Li-S cells with different separators were charged and discharged at 0.2C ($1\text{C} = 1,673 \text{ mA g}^{-1}$). The voltage plateaus of the Li-S cell with a $\text{Ti}_{0.87}\text{O}_2/\text{PP}$ separator (Figure S41) were consistent with its CV measurement. The initial discharge capacity was measured to be 960 mAh g^{-1} , followed by a moderate drop to 750 mAh g^{-1} by the end of the 500th cycle (Fig. 6a). In contrast, a cell

with a PP separator displayed an initial capacity of 980 mAh g^{-1} (Figure S42) and rapidly decreased to 345 mAh g^{-1} after 500 cycles. For the cells with the anatase TiO_2/PP (Figure S43) and GO/PP (Figure S44) separators, lower specific capacities of 450 and 580 mAh g^{-1} were obtained by the end of the 500th cycles, respectively. Figure S45 shows the rate performance of Li-S cells with $\text{Ti}_{0.87}\text{O}_2/\text{PP}$ and PP separators at different current rates from 0.2C to 2C. The charge-discharge profiles of cells with the $\text{Ti}_{0.87}\text{O}_2/\text{PP}$ separators showed distinguishable voltage plateaus at each current density (Figure S46). High specific capacities of 960 and 560 mAh g^{-1} were achieved at 0.2C and 2C, respectively. However, the cells with PP separators suffered from dramatic capacity decay. Although at 0.2C, the capacity reached up to 950 mAh g^{-1} , as the current rate was increased to 2C, the capacity dramatically decreased to 260 mAh g^{-1} . A long-term cycle test was conducted at a 1C rate for over 5000 cycles to verify the functioning of the $\text{Ti}_{0.87}\text{O}_2$ layer (Fig. 6b). A specific capacity of 585 mAh g^{-1} was maintained at the end of the 5000th cycle, corresponding to an ultralow capacity decay of 0.0036% per cycle. SEM images (Figure S47) showed that $\text{Ti}_{0.87}\text{O}_2$ nanosheets were still maintained on the separator after such long-term cycling. To the best of our knowledge, this is the best cycling stability among reported functionalized separators for Li-S batteries (Fig. 6c and Table S1), including GO ²⁸, graphene²⁹, G@PC ³¹, rGO@SL ³², CNT/NCQD ³³, MgAl-LDH ⁴¹, $\text{NiFe-LDH/N-graphene}$ ⁴⁰, $\text{MoS}_2\text{-PDDA/PAA}$ ³⁷, $\text{Sb}_2\text{Se}_{3-x}/\text{rGO}$ ²², Ti_3C_2 ³⁹, $\text{Cu}_2(\text{CuTCPP})$ ⁴⁴, CNT/ZIF-8 ⁴³, Ce-MOF/CNT ⁴⁵, BC/2D MOF-Co ⁴⁶, and Laponite nanosheets¹⁸.

To explore the potential for practical applications, thick cathodes with a sulfur loading of 3.5 mg cm^{-2} were assembled and investigated. Figure 6d shows the long-term cycling performance of a Li-S cell with a $\text{Ti}_{0.87}\text{O}_2/\text{PP}$ separator. After an initial activation at 0.2C, the cell delivered a specific capacity of 565 mAh g^{-1} at 1C up to 5000 cycles. Even at a high current density of 2C, this cell still delivered a reversible specific capacity of 250 mAh g^{-1} after 10000 cycles, corresponding to a capacity decay as low as 0.0035% per cycle. It should be noted that, to highlight the function of $\text{Ti}_{0.87}\text{O}_2$ nanosheets, the cathode matrix of carbon black has almost no PS adsorption ability. The use of porous carbon with hierarchical nanostructures as sulfur cathodes could further increase the sulfur mass loading for higher energy densities. For example, we used commercial carbon nanotubes (CNT) as the sulfur host (Figure S48). The Li-S batteries achieved high capacities and high area energy densities (Figures S49 and S50). Flexible Li-S pouch cells were assembled using $\text{Ti}_{0.87}\text{O}_2/\text{PP}$ separators. During charging and discharging at different bending angles, the pouch cells exhibited stable cycling performance at a current density of 0.2C up to 120 cycles (Fig. 6e).

The applications of $\text{Ti}_{0.87}\text{O}_2/\text{PP}$ separators was also extended for Li-Se batteries. Figures S51 and S52 show the typical charge/discharge profiles of Li-Se batteries with PP and $\text{Ti}_{0.87}\text{O}_2/\text{PP}$ separators, respectively. A gradually increased voltage polarization was observed for the Li-Se batteries with PP separators during the initial several cycles, accompanied by an obvious capacity decay. However, the overlapped charge/discharge curves confirmed the cycling stability of the Li-Se batteries with $\text{Ti}_{0.87}\text{O}_2/\text{PP}$ separators. After continuous cycling at 0.2C for over 500 cycles, a specific capacity of 460 mAh g^{-1} was

still retained (Figure S53). The $\text{Ti}_{0.87}\text{O}_2/\text{PP}$ separator is also promising to improve the cycling stability for Na-Se batteries. As shown in Figures S54 and S55, highly overlapped charge/discharge curves were observed for Na-Se batteries with $\text{Ti}_{0.87}\text{O}_2/\text{PP}$ separators, suggesting superior cycling performance compared to the cells with bare PP separators. Upon continuous cycling at 0.2C, a specific capacity of around 450 mA h g^{-1} was achieved after 250 cycles (Figure S56).

Discussion

In summary, we have demonstrated that 2D anionic $\text{Ti}_{0.87}\text{O}_2$ nanosheets with Ti atomic vacancies can be used as a selective ionic sieve with high permeability to regulate alkali metal (Li and Na) deposition while simultaneously preventing PS shuttling for alkali metal-S and alkali metal-Se batteries. The negatively charged $\text{Ti}_{0.87}\text{O}_2$ nanosheets showed strong electrostatic attraction and re-configurable adhesion for Li^+/Na^+ ions which enabled Li^+/Na^+ ions to transit rapidly. The Ti vacancies appear to act as sub-nanometre pores, providing fast diffusion channels for Li^+ or Na^+ -ions. Therefore, a homogeneous distribution of Li^+/Na^+ ions was achieved at the alkali metal anode side of test cells, inhibiting the growth of Li/Na dendrites without compromising the fast transport of Li^+/Na^+ ions. On the cathode side, the negatively charged $\text{Ti}_{0.87}\text{O}_2$ nanosheets showed strong electrostatic repulsion towards PS anions, resulting in effective suppression of PS shuttling. The $\text{Ti}_{0.87}\text{O}_2$ nanosheets enabled high-performance Li-S, Li-Se and Na-Se batteries with long cycle lives. Flexible Li-S pouch cells were assembled, showing stable cycling performance under different bending states. This work highlights a new strategy of using 2D nanosheets with atomic defects to achieve tandem control of migration of both cations and anions in advanced batteries.

Declarations

Competing Interests

The authors declare no competing interests.

Author Contributions

P.X., J.Z., and G.W. designed the research. P.X. and F.Z. conducted the synthesis, characterizations, and electrochemical measurements. P.X., X.Z. and J.S. performed the theoretical calculations. Y.L., Y.W., S.W. and B.S. helped the electrochemical measurements. Z.L. helped the microscopy characterizations. P.X., R.M., T.S., J.Z. and G.W. analysed and discussed the experimental results and drafted the manuscript. B.S., Z.L., Y.B. and X.W. joined the discussion of data and gave useful suggestions. P.X., F.Z. and X.Z. contributed equally to this work.

Acknowledgements

This work was supported by the Natural Science Foundation of China (No. 51902161, 51772152, 11574262), the Australian Research Council (ARC) through the Discovery Project program, (DP200101249) and the Fundamental Research Funds for the Central Universities (No. 30919011269). This work was also supported in part by the WPI-MANA, Ministry of Education, Culture, Sports, Science and Technology, Japan and CREST of the Japan Science and Technology Agency (JST).

References

1. Larcher, D. & Tarascon, J.-M. Towards greener and more sustainable batteries for electrical energy storage. *Nat. Chem.* **7**, 19–29 (2015).
2. Li, M., Lu, J., Chen, Z. & Amine, K. 30 years of lithium-ion batteries. *Adv. Mater.* **30**, 1800561 (2018).
3. Liu, B., Zhang, J.-G. & Xu, W. Advancing lithium metal batteries. *Joule* **2**, 833–845 (2018).
4. Manthiram, A., Fu, Y., Chung, S.-H., Zu, C. & Su, Y.-S. Rechargeable lithium-sulfur batteries. *Chem. Rev.* **114**, 11751–11787 (2014).
5. Pang, Q., Liang, X., Kwok, C.-Y. & Nazar, L.-F. Advances in lithium-sulfur batteries based on multifunctional cathodes and electrolytes. *Nat. Energy* **1**, 16132 (2016).
6. Abouimrane, A. *et al.* A new class of lithium and sodium rechargeable batteries based on selenium and selenium-sulfur as a positive electrode. *J. Am. Chem. Soc.* **134**, 4505–4508 (2012).
7. Yang, C.-P. *et al.* An advanced selenium-carbon cathode for rechargeable lithium-selenium batteries. *Angew. Chem. Int. Ed.* **52**, 8363–8367 (2013).
8. Manthiram, A., Fu, Y., Su, Y.-S. Challenges and prospects of lithium-sulfur batteries. *Acc. Chem. Res.* **46**, 1125–1134 (2013).
9. Evers, S. & Nazar, L.-F. New approaches for high energy density lithium-sulfur battery cathodes. *Acc. Chem. Res.* **46**, 1135–1143 (2013).
10. She, Z.-W., Sun, Y., Zhang, Q. & Cui, Y. Designing high-energy lithium-sulfur batteries. *Chem. Soc. Rev.* **45**, 5605–5634 (2016).
11. Ji, X., Lee, K.-T. & Nazar L.-F. A highly ordered nanostructured carbon-sulphur cathode for lithium-sulphur batteries. *Nat. Mater.* **8**, 500–506 (2009).
12. Zhou, G., Paek, E., Hwang, G.-S. & Manthiram, A. Long-life Li/polysulphide batteries with high sulphur loading enabled by lightweight three-dimensional nitrogen/sulphur-codoped graphene sponge. *Nat. Commun.* **6**, 7760 (2015).
13. Wang, J., He, Y.-S. & Yang, J. Sulfur-based composite cathode materials for high-energy rechargeable lithium batteries. *Adv. Mater.* **27**, 569–575 (2015).
14. Tao, T. *et al.* Anode improvement in rechargeable lithium-sulfur batteries. *Adv. Mater.* **29**, 1700542 (2017).
15. Cha, E. *et al.* 2D MoS₂ as an efficient protective layer for lithium metal anodes in high-performance Li-S batteries. *Nat. Nanotechnol.* **13**, 337–344 (2018).

16. Bai, S. *et al.* Metal-organic framework-based separator for lithium-sulfur batteries. *Nat. Energy* **1**, 16094 (2016).
17. Tu, S. *et al.* A polysulfide-immobilizing polymer retards the shuttling of polysulfide intermediates in lithium-sulfur batteries. *Adv. Mater.* **30**, 1804581 (2018).
18. Yang, Y. & Zhang, J. Highly stable lithium-sulfur batteries based on laponite nanosheet-coated celgard separators. *Adv. Energy Mater.* **8**, 1801778 (2018).
19. He, Y. *et al.* Simultaneously inhibiting lithium dendrites growth and polysulfides shuttle by a flexible MOF-based membrane in Li-S batteries. *Adv. Energy Mater.* **8**, 1802130 (2018).
20. Cheng, Z. *et al.* Separator modified by cobalt-embedded carbon nanosheets enabling chemisorption and catalytic effects of polysulfides for high-energy-density lithium-sulfur batteries. *Adv. Energy Mater.* **9**, 1901609 (2019).
21. Lu, Q. *et al.* An “electronegative” bifunctional coating layer: simultaneous regulation of polysulfide and Li-ion adsorption sites for long-cycling and “dendrite-free” Li-S batteries. *J. Mater. Chem. A* **7**, 22463–22474 (2019).
22. Tian, Y. *et al.* Low-bandgap Se-deficient antimony selenide as a multifunctional polysulfide barrier toward high-performance lithium-sulfur batteries. *Adv. Mater.* **32**, 1904876 (2020).
23. Li, Z. *et al.* Engineering oxygen vacancies in a polysulfide-blocking layer with enhanced catalytic ability. *Adv. Mater.* **32**, 1907444 (2020).
24. Yu, X., Bi, Z., Zhao, F. & Manthiram, A. Polysulfide-shuttle control in lithium-sulfur batteries with a chemically/electrochemically compatible NaSICON-type solid electrolyte. *Adv. Energy Mater.* **6**, 1601392 (2016).
25. Fan, L. *et al.* Simultaneous suppression of the dendrite formation and shuttle effect in a lithium-sulfur battery by bilateral solid electrolyte interface. *Adv. Sci.* **5**, 1700934 (2018).
26. Zhang, N., Li, B., Li, S. & Yang, S. Mesoporous hybrid electrolyte for simultaneously inhibiting lithium dendrites and polysulfide shuttle in Li-S batteries. *Adv. Energy Mater.* **8**, 1703124 (2018).
27. Li, S. *et al.* Inhibition of polysulfide shuttles in Li-S batteries: modified separators and solid-state electrolytes. *Adv. Energy Mater.* 2000779 (2020).
28. Huang, J.-Q. *et al.* Permselective graphene oxide membrane for highly stable and anti-self-discharge lithium-sulfur batteries. *ACS Nano* **9**, 3002–3011 (2015).
29. Zhou, G. *et al.* A flexible sulfur-graphene-polypropylene separator integrated electrode for advanced Li-S batteries. *Adv. Mater.* **27**, 641–647 (2015).
30. Zhai, P. Y. *et al.* Scaled-up fabrication of porous-graphene-modified separators for high-capacity lithium-sulfur batteries. *Energy Storage Mater.* **7**, 56–63 (2017).
31. Pei, F. *et al.* A two-dimensional porous carbon-modified separator for high-energy-density Li-S batteries. *Joule* **2**, 323–336 (2018).
32. Lei, T. *et al.* Inhibiting polysulfide shuttling with a graphene composite separator for highly robust lithium-sulfur batteries. *Joule* **2**, 2091–2104 (2018).

33. Pang, Y., Wei, J., Wang, Y. & Xia, Y. Synergetic protective effect of the ultralight MWCNTs/NCQDs modified separator for highly stable lithium-sulfur batteries. *Adv. Energy Mater.* **8**, 1702288 (2018).
34. Xiao, Z. *et al.* A lightweight TiO₂/graphene interlayer, applied as a highly effective polysulfide absorbent for fast, long-life lithium-sulfur batteries. *Adv. Mater.* **27**, 2891–2898 (2015).
35. Zhao, Y. *et al.* Dense coating of Li₄Ti₅O₁₂ and graphene mixture on the separator to produce long cycle life of lithium-sulfur battery. *Nano Energy* **30**, 1–8 (2016).
36. Ghazi, Z.-A. *et al.* MoS₂/celgard separator as efficient polysulfide barrier for long-life lithium-sulfur batteries. *Adv. Mater* **29**, 1606817 (2017).
37. Wu, J. *et al.* Ultralight layer-by-layer self-assembled MoS₂-polymer modified separator for simultaneously trapping polysulfides and suppressing lithium dendrites. *Adv. Energy Mater.* **8**, 1802430 (2018).
38. He, J., Chen, Y. & Manthiram A. Vertical Co₉S₈ hollow nanowall arrays grown on a celgard separator as a multifunctional polysulfide barrier for high-performance Li-S batteries. *Energy Environ Sci.* **11**, 2560–2568 (2018).
39. Song, J. *et al.* Immobilizing polysulfides with MXene-functionalized separators for stable lithium-sulfur batteries. *ACS Appl. Mater. Interfaces* **8**, 29427–29433 (2016).
40. Peng, H.-J. *et al.* A cooperative interface for highly efficient lithium-sulfur batteries. *Adv. Mater.* **28**, 9551–9558 (2016).
41. Zhou, Y. *et al.* Cationic two-dimensional sheets for an ultralight electrostatic polysulfide trap toward high-performance lithium-sulfur batteries. *Energy Storage Mater.* **9**, 39–46 (2017).
42. Zang, Y. *et al.* Large-area preparation of crack-free crystalline microporous conductive membrane to upgrade high energy lithium-sulfur batteries. *Adv. Energy Mater.* **8**, 1802052 (2018).
43. Wu, F. *et al.* Metal-organic frameworks composites threaded on the CNT knitted separator for suppressing the shuttle effect of lithium sulfur batteries. *Energy Storage Mater.* **14**, 383–391 (2018).
44. Tian, M. *et al.* Ultrathin MOF nanosheet assembled highly oriented microporous membrane as an interlayer for lithium-sulfur batteries. *Energy Storage Mater.* **21**, 14–21 (2019).
45. Hong, X.-J. *et al.* Cerium based metal-organic frameworks as an efficient separator coating catalyzing the conversion of polysulfides for high performance lithium-sulfur batteries. *ACS Nano* **13**, 1923–1931 (2019).
46. Li, Y. *et al.* Single atom array mimic on ultrathin MOF nanosheets boosts the safety and life of lithium-sulfur batteries. *Adv. Mater.* **32**, 1906722 (2020).
47. Cheng, C. *et al.* Low-voltage electrostatic modulation of ion diffusion through layered graphene-based nanoporous membranes. *Nat. Nanotechnol.* **13**, 685–690 (2018).
48. Zhang, M. *et al.* Controllable ion transport by surface-charged graphene oxide membrane. *Nat. Commun.* **10**, 1253 (2019).
49. Koenig, S.-P., Wang, L., Pellegrino, J. & Bunch, J.-S. Selective molecular sieving through porous graphene. *Nat. Nanotechnol.* **7**, 728–732 (2012).

50. Lin, L.-C. & Grossman, J.-C. Atomistic understandings of reduced graphene oxide as an ultrathin-film nanoporous membrane for separations. *Nat. Commun.* **6**, 8335 (2015).
51. Surwade, S.-P. *et al.* Water desalination using nanoporous single-layer graphene. *Nat. Nanotechnol.* **10**, 459–464 (2015).
52. Ding, L. *et al.* Effective ion sieving with $\text{Ti}_3\text{C}_2\text{T}_x$ MXene membranes for production of drinking water from seawater. *Nat. Sustain.* **3**, 296–302 (2020).
53. Sapkota, B. *et al.* High permeability sub-nanometre sieve composite MoS_2 membranes. *Nat. Commun.* **11**, 2747 (2020).
54. Sasaki, T. *et al.* Macromolecule-like aspects for a colloidal suspension of an exfoliated titanate. pairwise association of nanosheets and dynamic reassembling process initiated from it. *J. Am. Chem. Soc.* **118**, 8329–8335 (1996).
55. Sasaki, T. & Watanabe, M. Osmotic swelling to exfoliation. exceptionally high degrees of hydration of a layered titanate. *J. Am. Chem. Soc.* **120**, 4682–4689 (1998).
56. Wang, L. & Sasaki, T. Titanium oxide nanosheets: graphene analogues with versatile functionalities. *Chem. Rev.* **114**, 9455–9486 (2014).
57. Sasaki, T. *et al.* A mixed alkali metal titanate with the lepidocrocite-like layered structure. preparation, crystal structure, protonic form, and acid-base intercalation properties. *Chem. Mater.* **10**, 4123–4128 (1998).
58. Xiong, P. *et al.* Two-dimensional unilamellar cation-deficient metal oxide nanosheet superlattices for high-rate sodium ion energy storage. *ACS Nano* **12**, 12337–12346 (2018).
59. Ohwada, M. *et al.* Atomic structure of titania nanosheet with vacancies. *Sci. Rep.* **3**, 2801 (2013).
60. Angelomé, P.-C. *et al.* Mesoporous anatase TiO_2 films: use of Ti K XANES for the quantification of the nanocrystalline character and substrate effects in the photocatalysis behavior. *J. Phys. Chem. C* **111**, 10886–10893 (2007).
61. Pan, L. *et al.* Manipulating spin polarization of titanium dioxide for efficient photocatalysis. *Nat. Commun.* **11**, 418 (2020).
62. Fukuda, K. *et al.* Nanoarchitecture of semiconductor titania nanosheets revealed by polarization-dependent total reflection fluorescence X-ray absorption fine structure. *J. Phys. Chem. B* **108**, 13088–13092(2004).
63. Fukuda, K. *et al.* Colloidal unilamellar layers of tantalum oxide with open channels. *Inorg. Chem.* **46**, 4787–4789 (2007).
64. Xu, X. *et al.* Tantalum oxide nanomesh as self-standing one nanometre thick electrolyte. *Energy Environ. Sci.* **4**, 3509–3512 (2011).
65. Khurana, R., Schaefer, J.-L., Archer, L.-A. & Coates, G.-W. Suppression of lithium dendrite growth using cross-linked polyethylene/poly(ethylene oxide) electrolytes: a new approach for practical lithium-metal polymer batteries. *J. Am. Chem. Soc.* **136**, 7395–7402 (2014).

66. Tian, H. *et al.* Theoretical investigation of 2D layered materials as protective films for lithium and sodium metal anodes. *Adv. Energy Mater.* **7**, 1602528 (2017).
67. Guo, Y. *et al.* An autotransferable g-C₃N₄ Li⁺-modulating layer toward stable lithium anodes. *Adv. Mater.* **31**, 1900342 (2019).
68. Xu, Y. *et al.* Ion-transport-rectifying layer enables Li-metal batteries with high energy density. *Matter* **3**, 1685–1700 (2020).
69. Kovtyukhova, N.-I. *et al.* Layer-by-layer assembly of ultrathin composite films from micron-sized graphite oxide sheets and polycations. *Chem. Mater.* **11**, 771–778 (1999).

Figures

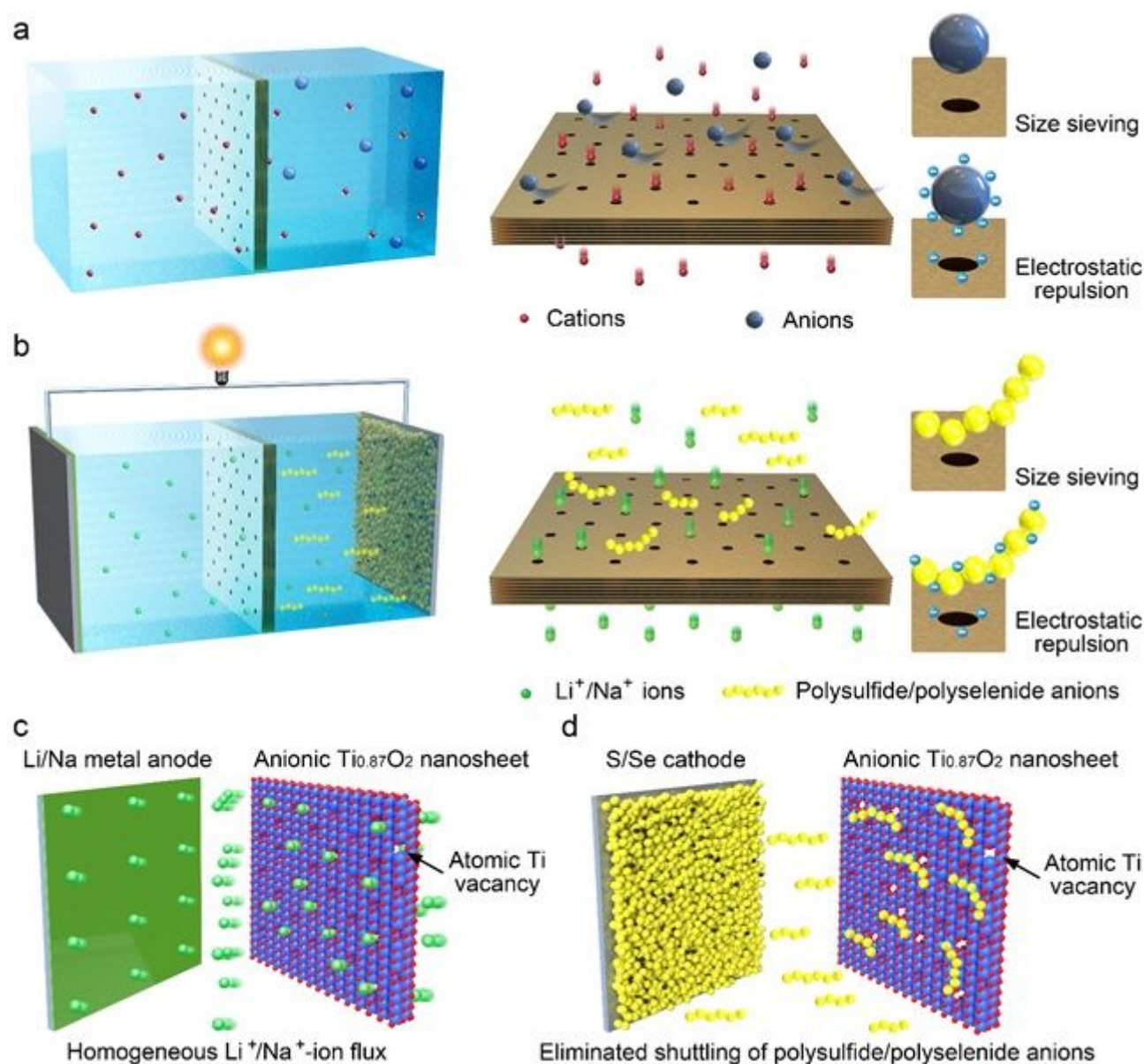


Figure 1

Schematic illustration of 2D porous nanosheets as a selective ionic sieve in membrane-based separation and alkali metal-S/Se batteries. (a) 2D porous nanosheet-based membranes act as selective ionic sieves in membrane-based separation technologies. The small cations can pass, while large anions are selectively excluded based on a size-sieving effect and electrical interaction between ions and membrane. (b) 2D nanosheets with sub-nanometer pores act as selective ionic sieves in alkali metal-S/Se batteries. The small Li^+/Na^+ ions can rapidly pass through the sub-nanopores, while the large polysulfide/polyselenide (PS) anions are selectively excluded due to size sieving effect and electrical repulsion between PS anions and negatively charged nanosheets. (c) 2D negatively charged $\text{Ti}_{0.87}\text{O}_2$ nanosheets with atomic Ti vacancies offer strong electrostatic interaction with Li^+/Na^+ ions, resulting in homogeneous distribution of Li^+/Na^+ -ion flux, preventing the growth of Li/Na dendrites. (d) 2D negatively charged $\text{Ti}_{0.87}\text{O}_2$ nanosheets with a high negative charge density provide a strong electrostatic repulsion of PS anions, resulting in effective suppression of PS shuttling.

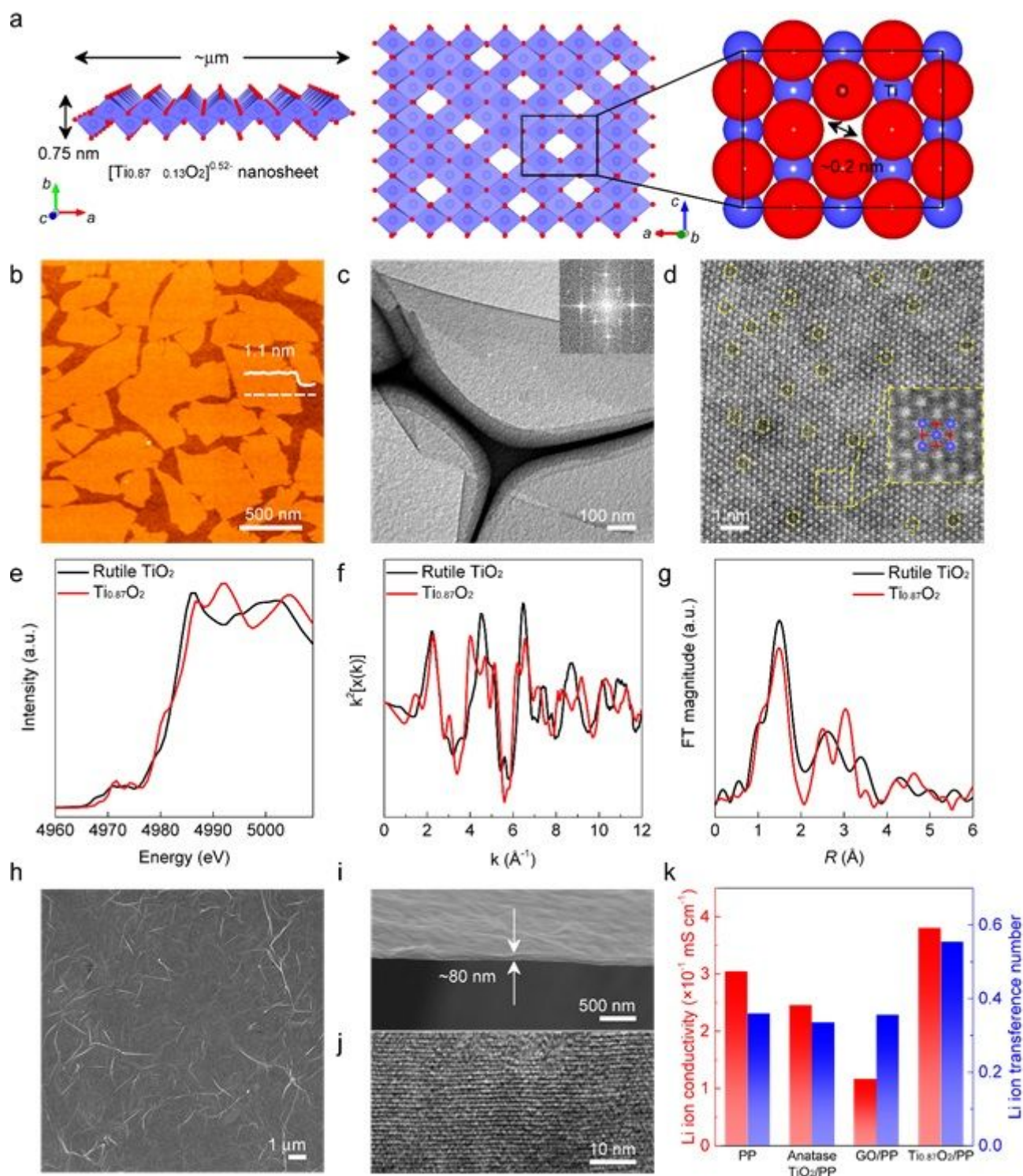


Figure 2

Fabrication and characterization of Ti_{0.87}O₂ nanosheets and Ti_{0.87}O₂/PP separators. (a) Crystal structures of Ti_{0.87}O₂ nanosheet with respect to c- and b-axes. Enlarged structure using ionic radii to show the relative size of the Ti vacancy. (b) AFM image of Ti_{0.87}O₂ nanosheets. (c) TEM image and SAED pattern of a Ti_{0.87}O₂ nanosheet. (d) HAADF-STEM image of a Ti_{0.87}O₂ nanosheet. (e) X-ray absorption near edge structure (XANES) of Ti K edge for commercial rutile TiO₂ and a freeze-dried sample of Ti_{0.87}O₂ nanosheets. (f) The k³-weighted EXAFS in K-space for commercial rutile TiO₂ and a

freeze-dried sample of $\text{Ti}_{0.87}\text{O}_2$ nanosheets. (g) Fourier transforms of k-space oscillations of Ti K edge of commercial rutile TiO_2 and a freeze-dried sample of $\text{Ti}_{0.87}\text{O}_2$ nanosheets. (h) SEM image showing a top-down view of a $\text{Ti}_{0.87}\text{O}_2/\text{PP}$ separator. (i) SEM image showing a side-on view of a $\text{Ti}_{0.87}\text{O}_2/\text{PP}$ separator. (j) TEM image showing a side view of a $\text{Ti}_{0.87}\text{O}_2/\text{PP}$ separator. (k) Li ion conductivity and Li ion transference number of PP, anatase TiO_2/PP , GO/PP and $\text{Ti}_{0.87}\text{O}_2/\text{PP}$ separators.

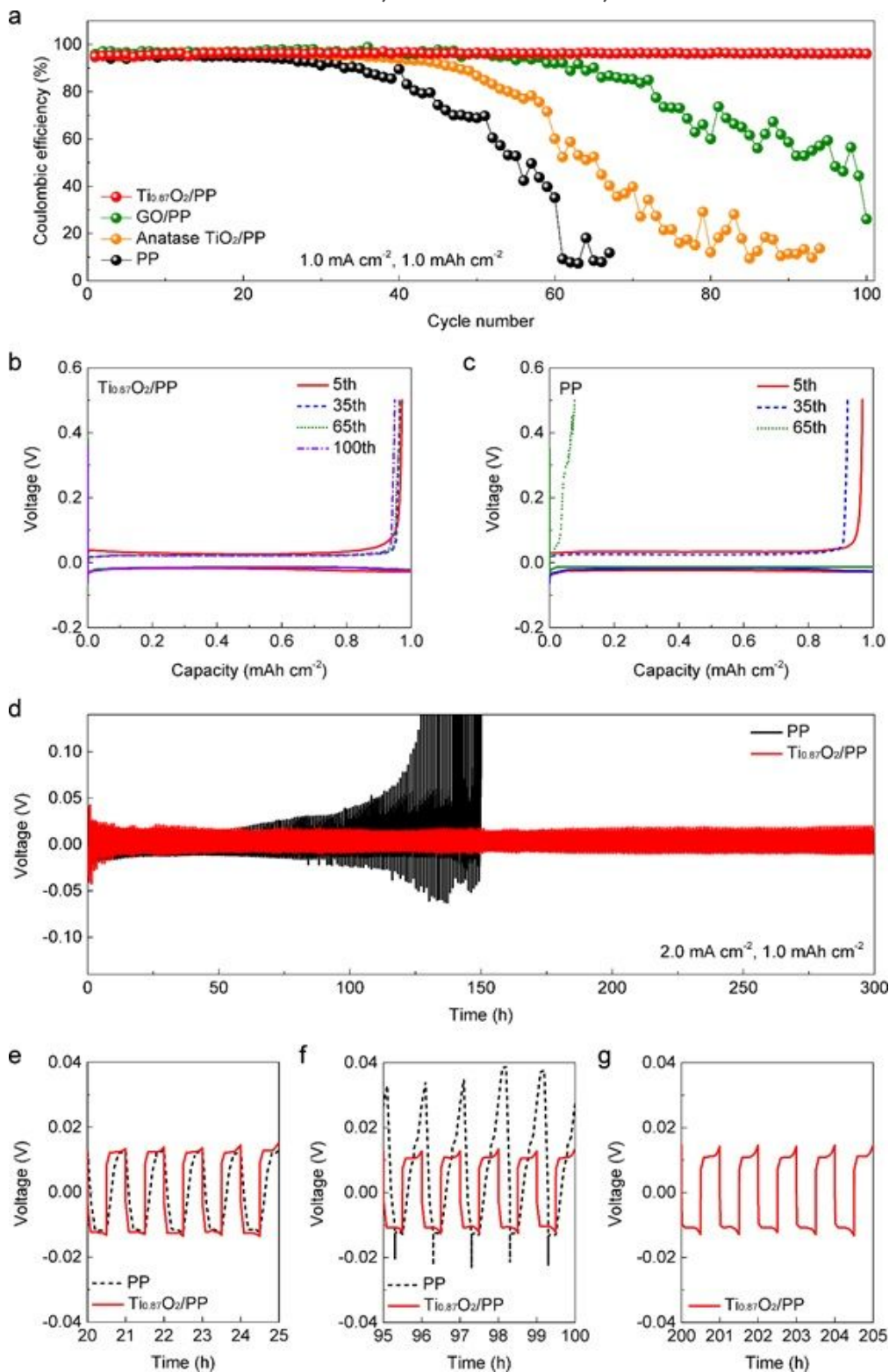


Figure 3

Electrochemical performance of Ti_{0.87}O₂/PP separator for dendrite-free Li metal anodes. (a) Coulombic efficiencies of Li||Cu cells with PP, anatase TiO₂/PP, GO/PP, and Ti_{0.87}O₂/PP separators with an area capacity of 1 mAh cm⁻² at 1 mA cm⁻². Voltage profiles of Li plating/stripping processes in Li||Cu cells with (b) Ti_{0.87}O₂/PP and (c) PP separators with an area capacity of 1 mAh cm⁻² at 1 mA cm⁻². (d) Voltage-time profiles of Li plating/stripping processes in Li||Li cells with PP and Ti_{0.87}O₂/PP separators with selected voltage-time profiles for the (e) 21st-25th, (f) 96th-100th, and (g) 201st-205th cycles.

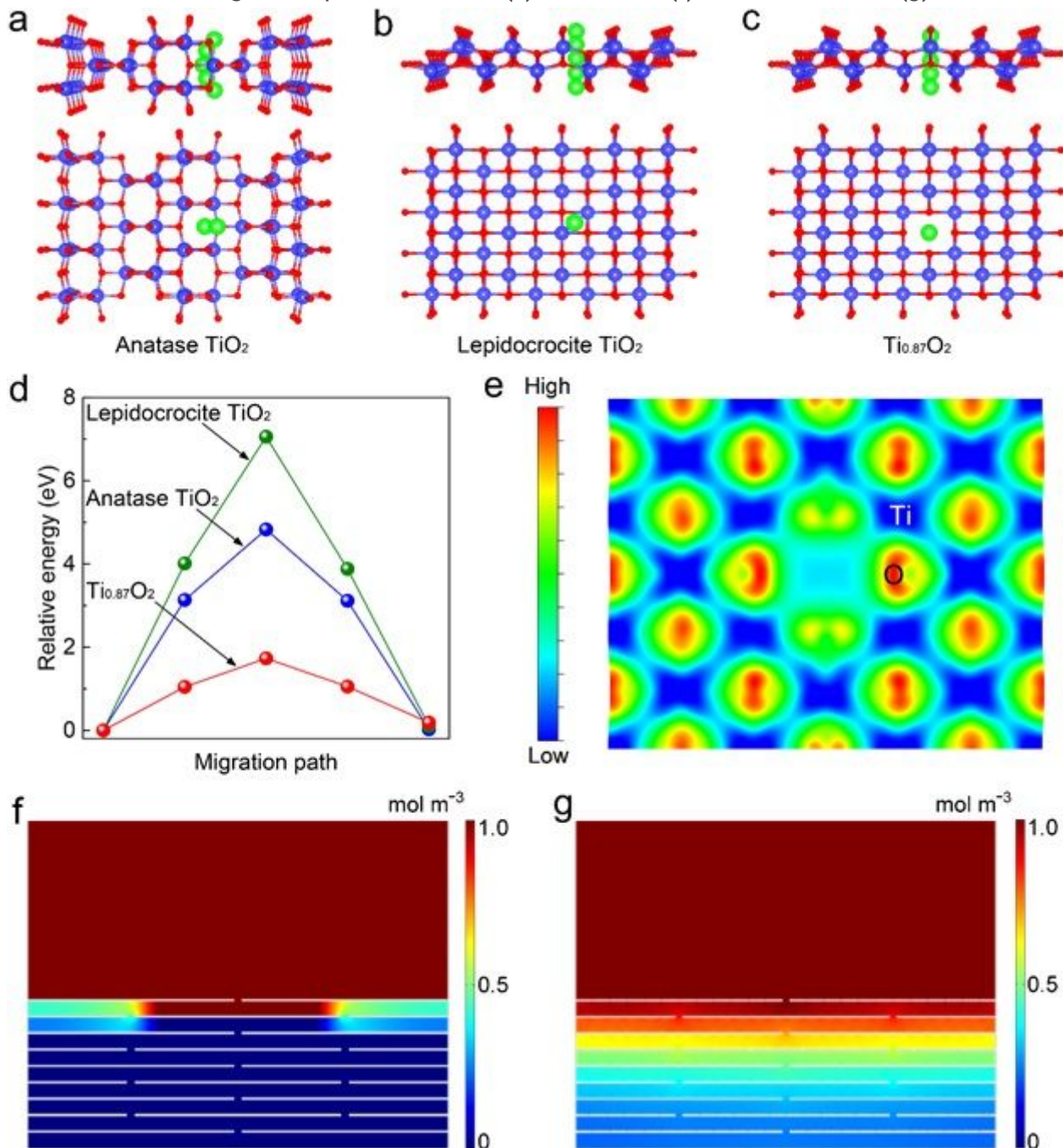


Figure 4

Theoretical calculations and simulation results of ion transportation behaviors in Ti_{0.87}O₂ nanosheets. Li⁺ ion diffusion in (a) anatase TiO₂, (b) lepidocrocite TiO₂ sheet, and (c) Ti-defective Ti_{0.87}O₂ sheet. (d) Potential-energy curves of Li⁺ ion diffusion in anatase TiO₂, lepidocrocite TiO₂, and Ti_{0.87}O₂. (e) Charge

density plot of $\text{Ti}_{0.87}\text{O}_2$ with a Ti defect. Distribution of Li^+ ions through a restacked thin layer of (f) conventional nanosheets and (g) Ti-defect nanosheets.

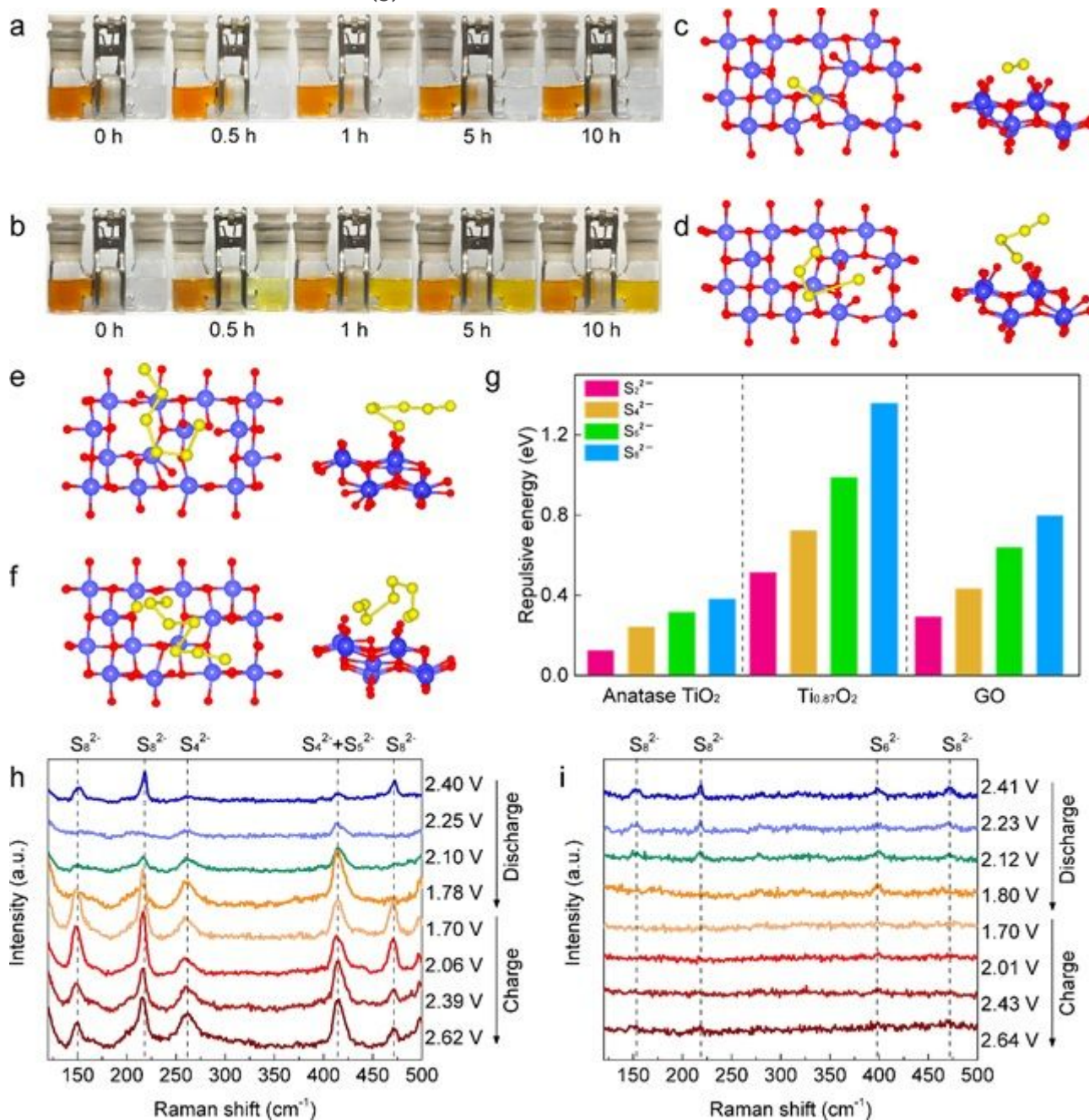


Figure 5

Polysulfide shuttling suppression capability for the $\text{Ti}_{0.87}\text{O}_2/\text{PP}$ separator. Polysulfide permeation measurements in H-type cells with (a) $\text{Ti}_{0.87}\text{O}_2/\text{PP}$ and (b) bare PP separators. Optimized conformations of (c) S_{22}^{2-} , (d) S_{42}^{2-} , (e) S_{62}^{2-} and (f) S_{82}^{2-} on a $\text{Ti}_{0.87}\text{O}_2$ sheet. (g) Repulsion energies of various polysulfide S_x^{2-} on anatase TiO_2 , GO and $\text{Ti}_{0.87}\text{O}_2$. Raman spectra obtained during the discharge and charge processes in Li-S batteries with (h) PP and (i) $\text{Ti}_{0.87}\text{O}_2/\text{PP}$ separators.

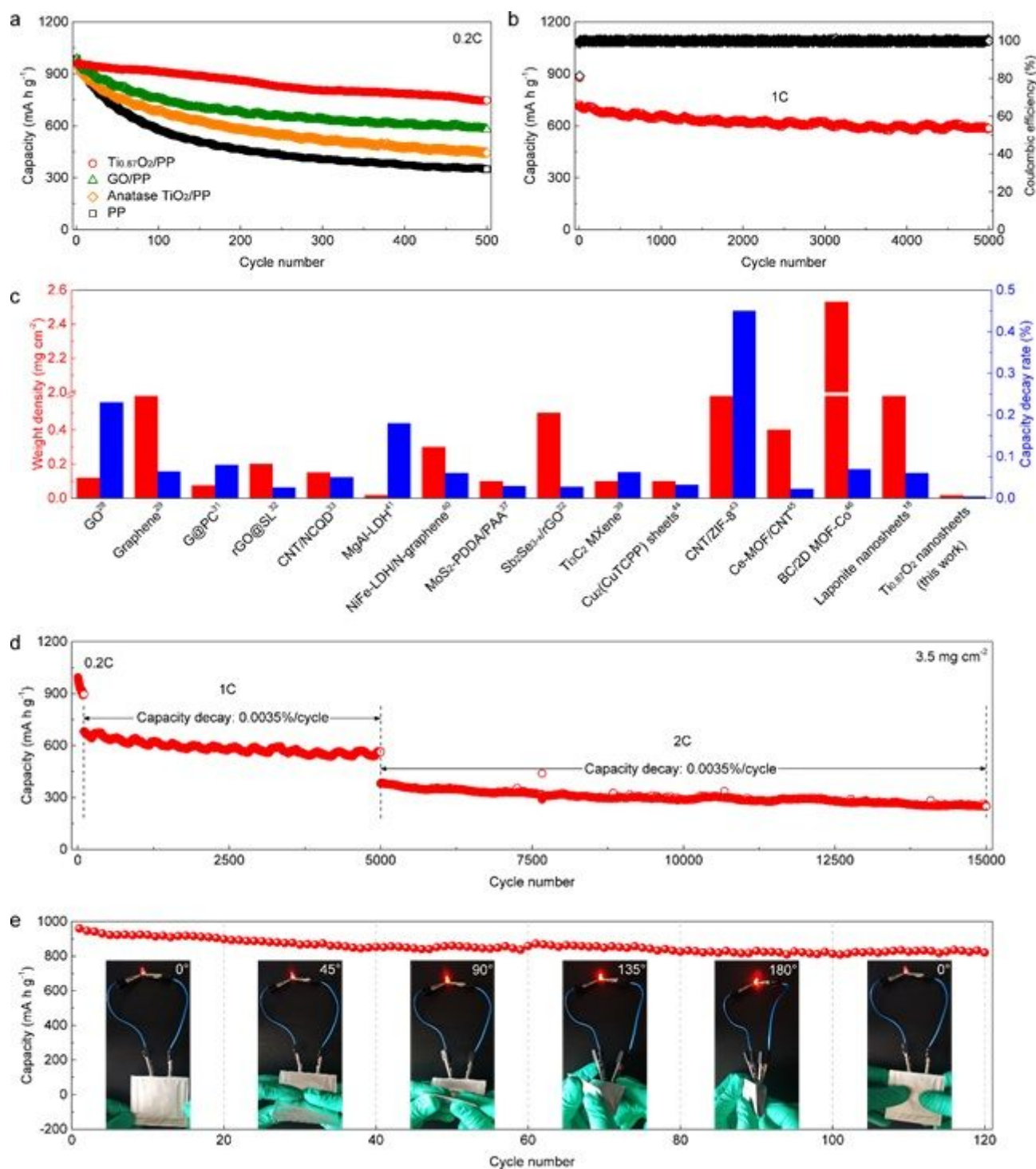


Figure 6

Li-S battery performance with $\text{Ti}_{0.87}\text{O}_2/\text{PP}$ separators. (a) Cycling performance with PP, anatase TiO_2/PP , GO/PP and $\text{Ti}_{0.87}\text{O}_2/\text{PP}$ separators at 0.2C for 500 cycles. (b) Long-term cycling stability of a Li-S battery with a $\text{Ti}_{0.87}\text{O}_2/\text{PP}$ separator at 1C for 5000 cycles. (c) Comparison of weight density and cycling performance for $\text{Ti}_{0.87}\text{O}_2$ nanosheets and some other reported functional layers on commercial separators in Li-S batteries. Further details of the selected functional materials are provided in the Supplementary Table S1. (d) Cycling performance of a Li-S battery with a $\text{Ti}_{0.87}\text{O}_2/\text{PP}$ separator at a

sulfur mass loading of 3.5 mg cm⁻². (e) Cycling performance of a flexible Li-S pouch cell with a Ti_{0.87}O₂/PP separator under different bending angles.

Supplementary Files

This is a list of supplementary files associated with this preprint. Click to download.

- [SupportingInformation.docx](#)
- [MoiveS1.mp4](#)